Energy Proceedings
Vol 60, 2025
ISSN 2004-2965

Numerical Investigation of Flow Properties in a Hollow Shaft of a Flywheel Energy Storage System under Vacuum Conditions

Jiao Yuanyuan[1, 2], Wang Yifei [1], Dai Xingjian [1*], Xu Yujie [1], Chen Haisheng [1, 2]

1 Institute of Engineering Thermophysics, Chinese Academy of Science, Beijing 100190, China

2 University of Chinese Academy of Sciences, Beijing 100049, China
(Corresponding Author: daixingjian@iet.cn)

ABSTRACT

This study numerically investigates the multiphase flow characteristics inside a hollow rotating shaft under near-vacuum conditions, aiming to clarify the fundamental flow mechanisms governing rotor cooling in flywheel energy storage systems (FESS). Computational fluid dynamics (CFD) simulations were conducted to compare the stationary and rotating configurations, focusing on the influence of shaft rotation on phase distribution, pressure evolution, and velocity field characteristics. In the stationary case, the impinging jet induces a strong local pressure peak and downward flow, accompanied by pronounced air entrainment, incomplete gas removal, and localized cavitation near geometric transitions. When rotation is introduced, centrifugal force dominates the flow dynamics, leading to a stable annular flow structure with liquid adhering to the wall and air confined to the shaft core. The air phase develops a helical backflow path driven by the low-pressure core region, while near-wall backflow and cavitation are significantly suppressed. The findings reveal a transition from a gravity- and inertia-driven, chaotic two-phase regime to a rotation-dominated, stratified annular flow regime. This transition enhances flow stability and liquid film continuity, offering important insights into the coupled flow-phase interactions under vacuum and providing practical guidance for the thermo-fluid optimization of high-speed flywheel rotors.

Keywords: Flywheel energy storage system (FESS); hollow rotating shaft; multiphase flow; near-vacuum flow; CFD simulation

NONMENCLATURE

Abbreviations	
CFD	Computational fluid dynamics
FESS	Flywheel energy storage system
PMSM	Permanent magnet synchronous motor
RANS	Reynolds-averaged Navier-Stokes
SST	Shear stress transport
TC	Taylor-Couette
TCP	Taylor-Couette-Poiseuille
Symbols	
f	body force
p	pressure
R_{B}	bubble radius
Re_{ax}	dimensionless axial flow Reynolds number
Re_{ω}	rotational flow Reynolds number
u	velocity
α	volume fraction
δ	annular gap width
μ_{t}	turbulent viscosity
ρ	density
τ_{ij}	viscous stress tensor
τ_{w}	wall shear stress
ω	angular velocity

1. INTRODUCTION

Flywheel energy storage systems (FESS) have attracted significant attention due to their ability to store energy in the form of rotational kinetic energy, offering high power density, fast response, and long service life[1-3]. Its basic structure is shown in *Fig. 1*, includes a rotating flywheel connected to a motor-generator, which can accelerate or decelerate the flywheel to store or release energy. When energy is stored, electrical power is converted into mechanical energy, causing the flywheel to spin. Upon discharge, the process is reversed, and the rotational energy is converted back into electrical power. Central to this process is the permanent magnet synchronous motor (PMSM), which is responsible for driving the flywheel during energy storage and extraction. While PMSMs offer high

This is a paper for the 5th Applied Energy Symposium and Forum: Renewable Energy Matrix (REM2025), Oct. 29-31, 2025, Yancheng, China.

efficiency and robustness, enabling high-speed operation critical for FESS, effective thermal management, particularly of the rotor, remains a fundamental challenge[4-6].

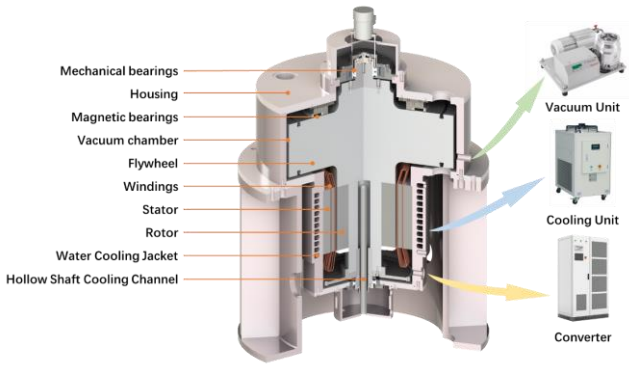

Fig. 1 A typical flywheel energy storage system

Heat generation within the rotor arises from core losses, eddy currents in permanent magnets, and frictional losses[7]. Excessive temperatures risk demagnetization, material degradation, thermal expansion-induced imbalance, and ultimately, system failure[8, 9]. Mitigating rotor heat buildup is especially complex in FESS. The necessity for a vacuum or low-pressure environment to minimize aerodynamic drag severely restricts conventional cooling methods like forced air or direct liquid cooling over the rotor surface.

To address this constraint, internal convective cooling via a hollow shaft has emerged as a promising solution, as illustrated in *Fig. 2*. The shaft is hollow, inside which a cantilevered pipe is installed. A tank filled with heat transfer fluid is positioned at the bottom. During operation, the fluid is circulated from the tank through the pipe into the hollow shaft using a pump. The circulating fluid absorbs the heat generated by the rotor and subsequently returns to the tank. The cooling system

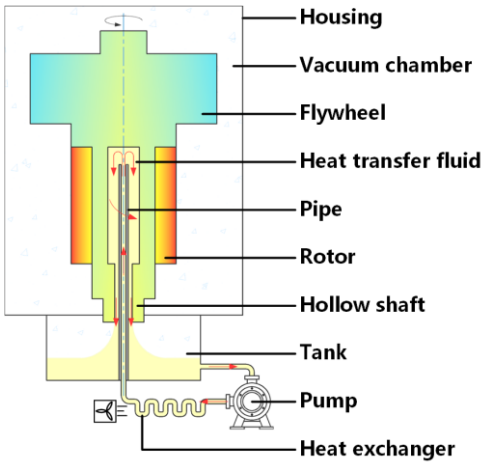

Fig. 2 A hollow shaft rotor cooling solution

is connected to a heat exchanger, which cools the thermal fluid and removes the absorbed heat. However, the low operating pressure creates a high propensity for cavitation at flow conditions, and the initial rarefied air induces complex multiphase flow within the shaft. The axial through-flow with high-speed rotation of the shaft, also known as Taylor-Couette-Poiseuille (TCP) flow, leads to intricate secondary flows. These phenomena critically influence flow distribution, residence time near hot surfaces, and crucially, induce substantial parasitic torque on the shaft and high flow pressure loss, consuming valuable energy intended for storage.

Despite investigations into TCP flow, significant limitations exist concerning the specific challenges of the FESS cooling system. Existing TCP research has primarily focused on fundamental flow characteristics and stability under controlled conditions. Studies have examined linear stability for various configurations, including co-rotation of cylinders at different speeds[10], eccentric rotation[11], and varying radius ratios[12]. Simulations by Poncet et al.[13] and Çoşgun et al.[14] for inner cylinder rotation have analyzed mean velocity profiles and turbulence intensity across combinations of rotational and axial Reynolds numbers. The influence of sudden annular contractions/expansions on Taylor vortex propagation and pressure oscillations has been explored[15], while experiments demonstrated how axial flow promotes the formation of spiral vortex structures[16]. Crucially, the vast majority of this work addresses inner cylinder rotation, with research on outer cylinder rotation being notably scarce. Yoo[17] studied TC flow without axial flow under outer cylinder rotation, observing flow regimes categorized by vortex count. Hadžiabdić et al.[18] employed LES to investigate fully developed turbulent flow in a concentric annulus with a rotating outer wall, highlighting the impact of rotation rate on turbulence and suggesting a ratio of centrifugal to axial inertial forces as a potential regime criterion.

Research incorporating multiphase flow and cavitation within rotating flows is even more limited and predominantly confined to simpler Taylor-Couette (TC) systems. Verschoof et al.[19] experimentally demonstrated that cavitation promoters on the inner cylinder generated bubbles, reducing drag. Teamah et al.[20] investigated transient flow fields with varying oil levels in a horizontal TC apparatus for enhanced thermal performance. Reinke et al.[21] utilized high-speed imaging to record cavitation and PIV for velocity field measurements to analyze cavitation behavior induced by inner cylinder rotation. While Wang et al.[22] studied flow and heat transfer in a structure somewhat similar to

the present cooling system, their focus was primarily on thermal aspects, and key flow path dimensions were unspecified. Pan et al.[23] employed sidewall jetting, resulting in a fundamentally different flow structure. Critically, both papers assumed fully flooded, single-phase conditions, neglecting multiphase effects under vacuum.

Existing research on TCP flow predominantly operates under atmospheric pressure, considers only single-phase flow, and employs simplified geometries devoid of complex internal features. Similarly, studies on cavitation typically neglect the profound influence of coupled axial-rotational flow dynamics and intricate geometric constraints. Consequently, a significant and largely unaddressed knowledge gap exists concerning the complex liquid-vapor-air three-phase flow dynamics within the specific geometry of a hollow shaft featuring a cantilevered pipe. This regime inherently involves incomplete filling and recirculating liquid flow patterns, vacuum-induced cavitation under near-saturation conditions, and intense, outer-cylinder-dominated TCP flow. The lack of validated understanding and predictive capability for this multiphase, rotating coupled flow regime under vacuum directly hampers the reliable design and optimization of energy-efficient hollow-shaft cooling systems for high-speed FESS rotors operating in vacuum environments.

This study employs high-fidelity CFD simulations to investigate the multiphase flow behavior within a hollow rotating shaft under near-vacuum conditions, with a particular emphasis on comparing stationary and 1000 rpm rotating configurations. The analysis focuses on how rotation influences phase distribution, pressure fields, and velocity characteristics, as well as the potential onset of cavitation phenomena. By establishing a connection between qualitative flow structures and quantitative flow features, this work provides a comprehensive understanding of the coupled flow-phase interactions and offers practical guidance for the thermo-fluid optimization of high-speed flywheel rotors.

2. METHODS

2.1 Physical model

To simulate the flow characteristics of the fluid inside the hollow shaft under vacuum conditions, the complex shafting was simplified. A tapered sleeve was added to the outlet section of the hollow shaft flow channel to reduce the tangential velocity of the exiting fluid. The simplified physical model of the hollow shaft rotor cooling system is shown in *Fig. 3*, with dimensional parameters listed in *Table 1*. The rotor shafting assembly rotates at a constant angular speed ω, while the pipe remains stationary. A heat transfer fluid at temperature T_{i} flows vertically into the hollow shaft from the pipe inlet at a constant velocity u_{i}. The surrounding environment is a low-pressure region maintained at a constant pressure $p_0 = 25\mathrm{Pa}$.

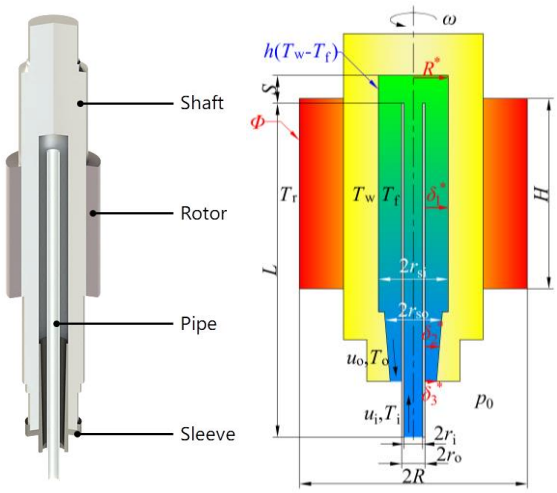

Fig. 3 Model of the hollow shaft rotor cooling system

Table 1 Dimensional parameters of the model

	Parameters	Symbols	Values (mm)
1	Inside diameter of the pipe	$2r_{\mathrm{i}}$	18.71
2	Outside diameter of the pipe	$2r_{\mathrm{o}}$	21.25
3	Distance from the top of the pipe to the top inside the hollow shaft	S	29
4	Diameter of the flow channel in the hollow shaft	$2r_{\mathrm{si}}$	50
5	Diameter of the flow channel in the hollow shaft at the outlet	$2r_{\mathrm{so}}$	44→36
6	Rotor diameter	$2R$	150
7	Rotor height	H	218
8	Pipe length	L	550

The Properties of the materials used for numerical modeling are provided in *Table 2*. Due to the low ambient pressure, the heat transfer oil may cavitate. The saturated vapor pressure of the heat conducting oil vapor is 2×10^{-5} Pa at 20 °C.

Table 2 Properties of the materials

	Air	Oil	Oil vapor
Density ($\mathrm{kg\cdot m^{-3}}$)	ideal gas	823.8	ideal gas
Dynamic viscosity ($\mathrm{kg\cdot m^{-1}\cdot s^{-1}}$)	1.846×10^{-5}	0.02812	2×10^{-5}

2.2 Governing Equations

For the flow in the hollow shaft, the governing equations are derived from the Reynolds-averaged Navier-Stokes (RANS) equations, which are applied to account for turbulent flow behavior.

1) Continuity equation

$$\frac{\partial \rho_{\mathrm{m}}}{\partial t}+\frac{\partial\left(\rho_{\mathrm{m}} \bar{u}_{\mathrm{m},j}\right)}{\partial x_j}=0 \tag{1}$$

where ρ_{m} is the mixture density, and $\bar{u}_{\mathrm{m},j}$ is the mass-averaged velocity component in the j-th direction.

2) Momentum equations

The momentum equation for the mixture can be obtained by summing the individual momentum equations for all phases. A single-phase momentum equation is

$$\frac{\partial(\rho \bar{u}_i)}{\partial t}+\frac{\partial\left(\rho \bar{u}_i \bar{u}_j\right)}{\partial x_j}=-\frac{\partial \bar{p}}{\partial x_i}+\frac{\partial \tau_{ij}}{\partial x_j}+\frac{\partial\left(-\rho \overline{u_i' u_j'}\right)}{\partial x_j}+\rho f_i \tag{2}$$

where $\bar{p}$ is the time-average pressure; τ_{ij} is the viscous stress tensor; $-\rho \overline{u_i' u_j'}$ represent the Reynolds stresses; f_i is the body force.

3) Turbulence model equations

The shear stress transport (SST) k−ω turbulence model is employed for accurately predicting turbulence effects[24-27], especially in near-wall regions:

$$\frac{\partial(\rho k)}{\partial t}+\frac{\partial\left(\rho k \bar{u}_j\right)}{\partial x_j}=\frac{\partial}{\partial x_j}\left[\left(\mu+\frac{\mu_{\mathrm{t}}}{\sigma_k}\right)\frac{\partial k}{\partial x_j}\right]+P_k-\rho \beta^* k \omega \tag{3}$$

$$\frac{\partial(\rho \omega)}{\partial t}+\frac{\partial\left(\rho \omega \bar{u}_j\right)}{\partial x_j}=\frac{\partial}{\partial x_j}\left[\left(\mu+\frac{\mu_{\mathrm{t}}}{\sigma_\omega}\right)\frac{\partial \omega}{\partial x_j}\right]+\frac{\gamma}{\nu_t}P_k-\rho \beta \omega^2+2(1-F_1)\frac{\rho}{\omega \sigma_{\omega 2}}\frac{\partial k}{\partial x_j}\frac{\partial \omega}{\partial x_j} \tag{4}$$

4) Multiphase flow equations

To accurately capture cavitation phenomena within the flow, the multiphase Mixture model was employed, which maintains simulation fidelity while reducing computational complexity. From the continuity equation, the volume fraction equation for secondary phase r can be obtained:

$$\frac{\partial\left(\rho_r \alpha_r\right)}{\partial t}+\frac{\partial\left(\rho_r \alpha_r \bar{u}_{\mathrm{m},j}\right)}{\partial x_j}=-\frac{\partial\left(\rho_r \alpha_r\left(\bar{u}_{\mathrm{dr},r}\right)_j\right)}{\partial x_j}+\sum_{s=1}^{n}\left(\dot{m}_{sr}-\dot{m}_{rs}\right) \tag{5}$$

where $\bar{u}_{\mathrm{dr},r}$ is the drift velocity of the phase r; $\dot{m}_{sr}$ and $\dot{m}_{rs}$ are the mass transfer from phase s to r and from phase r to s, respectively. The Mixture model treats the multiphase flow as a quasi-single-phase continuum in which all phases share a common velocity field but allow interphase slip velocities. The velocity of phase r relative to phase s is defined as:

$$\vec{u}_{rs}=\vec{u}_r-\vec{u}_s \tag{6}$$

The Schnerr-Sauer model is selected for its physically grounded representation of bubble dynamics in low-pressure environments and superior convergence behavior in rotating reference frame simulations. Expressions of the mass transfer rate R are:

$$\begin{cases} R_{\mathrm{e}}=F_{\mathrm{vap}}\dfrac{\rho_{\mathrm{v}}\rho_{\mathrm{l}}}{\rho}\alpha(1-\alpha)\dfrac{3}{R_{\mathrm{B}}}\sqrt{\dfrac{2}{3}\dfrac{p_{\mathrm{v}}-p}{\rho_{\mathrm{l}}}}, & p_{\mathrm{v}}>p \\ R_{\mathrm{c}}=F_{\mathrm{cond}}\dfrac{\rho_{\mathrm{v}}\rho_{\mathrm{l}}}{\rho}\alpha(1-\alpha)\dfrac{3}{R_{\mathrm{B}}}\sqrt{\dfrac{2}{3}\dfrac{p-p_{\mathrm{v}}}{\rho_{\mathrm{l}}}}, & p_{\mathrm{v}}\le p \end{cases} \tag{7}$$

where F_{vap} and F_{cond} are the empirical calibration coefficients of evaporation and condensation with the default value of 1 and 0.2, respectively; R_{B} is the bubble radius; α is the vapor volume fraction; ρ_{v} and ρ_{l} are the vapor and liquid density, respectively; ρ is the mixture density, which is defined as

$$\rho=\alpha\rho_{\mathrm{v}}+(1-\alpha)\rho_{\mathrm{l}} \tag{8}$$

2.3 Mesh and Solver Settings

For both the fluid and the solid domain in the hollow-shaft internal flow and heat transfer process, hexahedral structured meshes were generated as shown in Fig. 4. To satisfy the requirement of SST k-ω turbulence model for resolving the viscous sublayer, the near-wall mesh was appropriately refined to ensure a boundary layer $y^+\approx 1$. The value of y^+ can be calculated by the following equations:

$$v^*=\sqrt{\frac{\tau_{\mathrm{w}}}{\rho}} \tag{9}$$

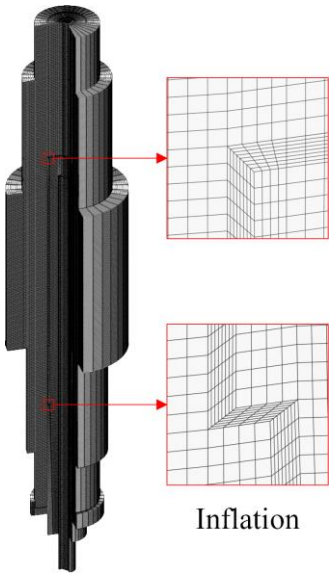

Fig. 4 Mesh of the hollow shaft structure

$$y^+ = \frac{\rho v^* y}{\mu} \tag{10}$$

where v^* is the friction velocity; τ_w is the wall shear stress; y is the normal distance to the wall.

This study utilizes Fluent to perform coupled fluid-thermal simulations. To ensure the reliability and accuracy of the numerical results, grid-independence tests were performed with various mesh-refinement strategies. Three-dimensional steady calculations employed the coupled solver, and the working fluid was initialized as rarefied air. Upon increasing the mesh to 3.2 million cells, the volume fraction of liquid phase and y^+ at the principal monitoring points converged to stable values, thereby accurately capturing the flow condition. Consequently, this mesh configuration was adopted for all subsequent simulations.

A moving reference frame was used to simulate the rotation of the shaft assembly. Mass-flow-inlet and pressure-outlet boundary conditions were imposed. A coupled-solution approach was adopted to solve the Navier-Stokes equations, volume fraction equations, slip velocity equations and turbulence equations simultaneously. Inlet and outlet mass flow rates, wall shear stress and phase distribution were monitored. The solution was considered converged when all equations residuals remained stable, and the monitored physical quantities exhibited no further variation with additional iterations.

2.4 Flow Conditions

For the hollow-shaft rotor cooling system with fixed geometric dimensions, the flow characteristics of the fluid inside the shaft vary with different inlet mass flow rates and shafting rotational speeds. The axial and rotational components of the flow velocity are characterized using the dimensionless axial flow Reynolds number Re_{ax} and rotational flow Reynolds number Re_ω, respectively:

$$Re_{ax} = \frac{2\rho u \delta}{\mu} \tag{11}$$

$$Re_\omega = \frac{\rho \omega r_{out} \delta}{\mu} \tag{12}$$

where u is the characteristic axial velocity; ω is the angular velocity; $\delta = r_{si} - r_o$ denotes the annular gap width. Notably, when the fluid does not completely occupy the annulus, for example, a thin film with a thickness of d is formed and attached to the outer cylinder wall, where $d < \delta$, the characteristic length of dimensionless numbers must be modified. However, it is challenging because calculations reveal that the liquid-phase thickness varies along the axial direction. Consequently, δ was still used in this article to define Re_{ax} and Re_ω.

2.5 Model Validation

To verify the reliability of the present computational model, a validation was performed based on the study by Hadžiabdić et al.[18], which investigated the TCP flow under conditions of axial through-flow and rotating outer cylinder. Although the original work used air as the working fluid and a horizontally oriented configuration, the present model adopts a vertically aligned geometry but maintains the same fluid properties and flow regime for consistency.

Three representative cases were selected for comparison, corresponding to different outer cylinder rotation speeds while keeping the Re_{ax} fixed at 12500. The Re_ω was set as 3125, 6250, and 12500, respectively, matching the dimensionless parameters in the reference study. The annular gap δ between the cylinders was 0.02875 m, with an inner stationary cylinder and a rotating outer cylinder. The flow domain was simplified by removing the inlet pipe, and the top surface was set as a uniform velocity inlet, while the bottom was treated as a pressure outlet. Gravity was not considered.

The simulations were carried out using the SST k-ω turbulence model. The fluid was treated as incompressible and isothermal, with constant physical properties. The mesh quality was carefully controlled to resolve near-wall gradients adequately, and the dimensionless wall distance was maintained $y^+ \approx 1$ in all regions.

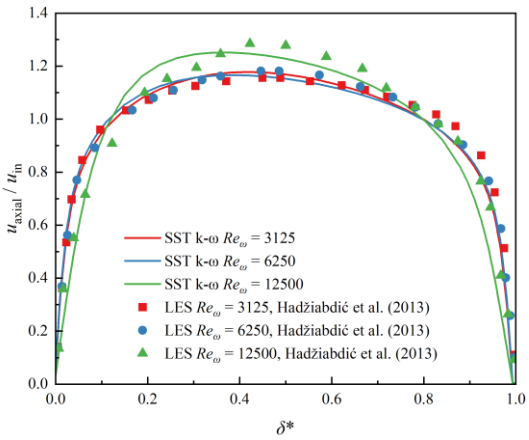

Fig. 5 Results of the model validation

Fig. 5 compares the non-dimensionalized mean axial velocity profile as a function of the non-dimensional radius for all cases. The results obtained from the present simulations show good agreement with the reference data. The deviations in velocity magnitude

were found to be less than 0.1, indicating the adequacy of the numerical settings and validating the model's ability to capture the essential physics of TCP flow under the tested conditions. This validated model provides a solid foundation for the multiphase and cavitating flow simulations presented in the subsequent sections.

3. RESULTS AND DISCUSSION

3.1 Stationary Hollow Shaft

Fig. 6 illustrates the flow characteristics under the stationary shaft condition, including the liquid phase distribution, absolute pressure field, inlet streamlines, and outlet recirculation streamlines. Under the pressure difference between the inlet and the outlet, the heat transfer oil jet impinges on the inner top wall of the hollow shaft, producing a distinct local pressure peak. In the absence of centrifugal forces, the driving momentum of the oil jet is insufficient at low axial velocities to sustain a continuous radial spreading along the top wall. Consequently, part of the oil departs prematurely from the top surface under the influence of gravity and directly impinges on the sidewall. The impingement and subsequent deflection of the liquid generate a weak recirculation region near the junction of the top wall and the sidewall, where a small portion of the liquid flows upward, entraining and replacing part of the initially trapped air. However, a thin air layer remains in this corner region, indicating incomplete air displacement during the filling process.

Most of the liquid subsequently flows downward along the sidewall. Due to the relatively low flow rate and the intermittent splashing caused by jet impingement, liquid droplets become entrained in the surrounding air, forming a liquid-air two-phase flow. When the two-phase mixture reaches the outlet sleeve with an abrupt contraction, the kinetic energy is partially converted into pressure energy, and the local static pressure recovers to approximately 140 Pa. After impingement on the contraction section, the liquid undergoes a short horizontal movement followed by a ballistic trajectory before attaching to the converging wall downstream. At the junction between the sudden contraction and the converging section, continuous removal of air without replenishment leads to a local pressure minimum, where cavitation occurs.

At the outlet, the low pressure within the hollow shaft induces a high-speed air backflow along the wall of the pipe. The backflow persists until the total pressure becomes lower than that of the incoming two-phase mixture, after which the air reverses direction and is expelled from the hollow shaft. Under the compressive effect of the backflowing air, the two-phase mixture flows downstream along the converging wall, where the near-wall region transitions into an almost pure liquid phase. Excluding the outlet pipe, the average volume

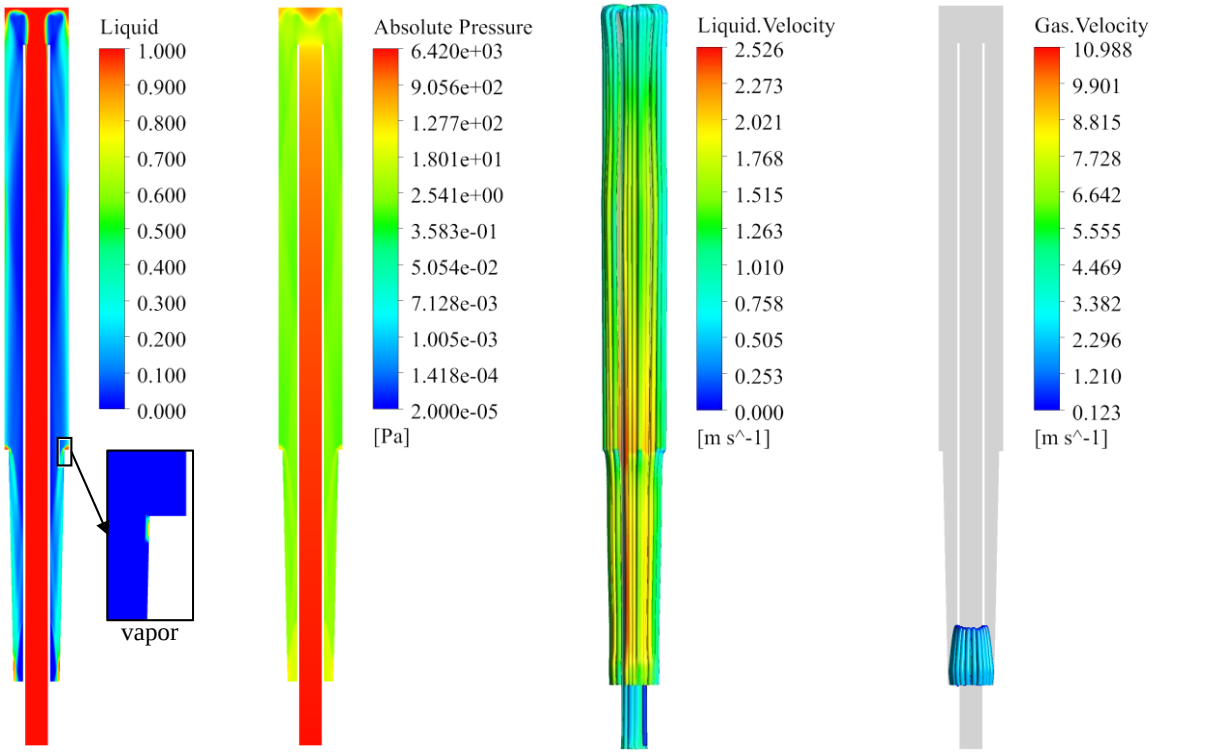

(a) liquid volume fraction (b) absolute pressure (c) streamline - oil flow (d) streamline - reserve flow

Fig. 6 Flow characteristics under the stationary shaft condition

fractions of the liquid, air, and vapor phases within the hollow shaft are 17.87%, 82.13%, and < 0.01%, respectively.

To further analyze the flow behavior, *Fig. 7* presents the distributions of axial velocity and liquid volume fraction along the dimensionless radial R^* or δ^* coordinate at 4 axial positions: near the top surface, in the mid-section of the hollow shaft, at the mid-section of the sleeve, and at the outlet, as shown by the red line in *Fig. 3*. For the near-top surface, the radial velocity is analyzed instead of the axial velocity.

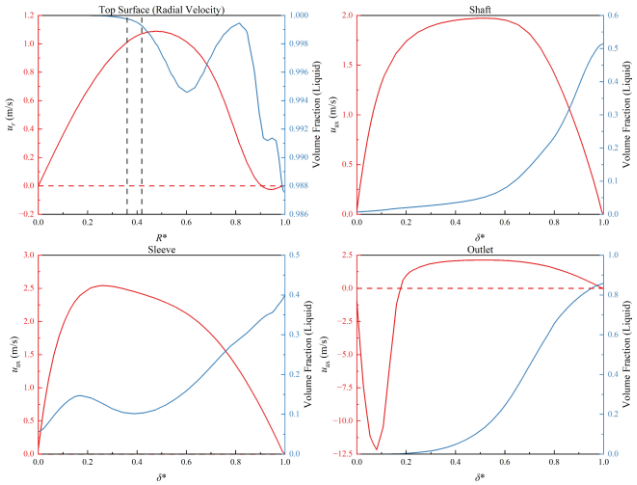

Fig. 7 Distributions of axial velocity and liquid volume fraction

Near the top wall, the jet center velocity is nearly zero, and the radial velocity increases with radius, reaching its maximum in the mid-region. Close to the sidewall, a weak reverse flow is observed, with a velocity magnitude below 0.1 m/s. The liquid phase dominates this region, with a volume fraction exceeding 98%. As the radius increases, the liquid fraction gradually decreases but exhibits a secondary peak near the sidewall, which is attributed to the local liquid backflow.

In the mid-section of the hollow shaft, the velocity profile exhibits a typical parabolic shape. Due to the higher liquid volume fraction near the wall region (exceeding 50%), the boundary layer thickness is larger than that near the pipe wall. In the mid-section of the sleeve, the local contraction of the flow area leads to an increase in velocity, accompanied by a rise in liquid fraction near the pipe wall. At the outlet, a pronounced air backflow is observed, reaching a velocity of up to 12 m/s, although this motion is confined to the region adjacent to the pipe. Outside this region, the velocity magnitude remains similar to that within the sleeve.

3.2 Rotating Hollow Shaft

Fig. 8 illustrates the flow characteristics under the rotating shaft condition. When a constant rotational speed of 1000 rpm is applied to the hollow shaft, the jet flow from the pipe outlet exhibits a similar pattern to that in the stationary case. However, the overall flow

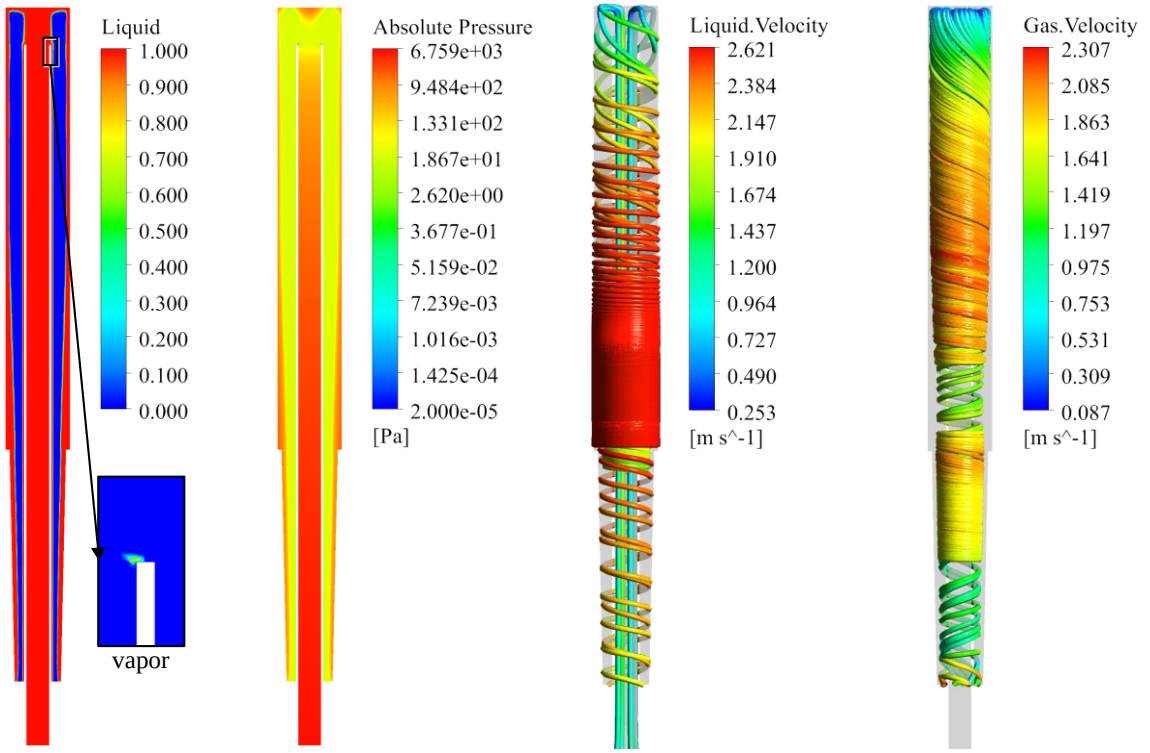

(a) liquid volume fraction (b) absolute pressure (c) streamline - oil flow (d) streamline - reserve flow

Fig. 8 Flow characteristics under the rotating shaft condition

behavior is significantly modified by centrifugal effects. Driven by centrifugal forces, the oil film spreads smoothly along the top wall and reaches the sidewall, eliminating the backflow observed in the stationary configuration. Centrifugal force dominates the two-phase distribution inside the rotating shaft, forming an annular flow regime. The liquid phase is forced toward the sidewall, while the gas phase is confined near the axis due to phase separation. A small portion of oil, unable to reach the top surface, flows downward along the outer wall of the inlet pipe, forming a small cavitation zone.

At the upper end of the sleeve, where a sudden cross-sectional contraction occurs, the circumferential oil flow is locally blocked, resulting in transient liquid accumulation. The strong radial pressure gradient generated by rotation produces a higher pressure near the wall and a lower pressure near the axis. Consequently, the gas within the core is gradually entrained downward and then drawn toward the outlet. The pressure reduction inside the shaft induces an air backflow from the outlet, which moves helically upward along the shaft axis under the influence of the rotating liquid phase. Under this condition, the volume fractions of the liquid and air phases inside the hollow shaft are 45.03% and 54.97%, respectively.

The axial velocity and liquid volume fraction distributions for the rotating condition are illustrated in Fig. 10. Near the top surface, the radial velocity profile remains similar to that of the stationary case, except that no backflow is observed. The flow is dominated by a single-phase liquid jet, indicating that the centrifugal force assists the oil in fully spreading over the top wall.

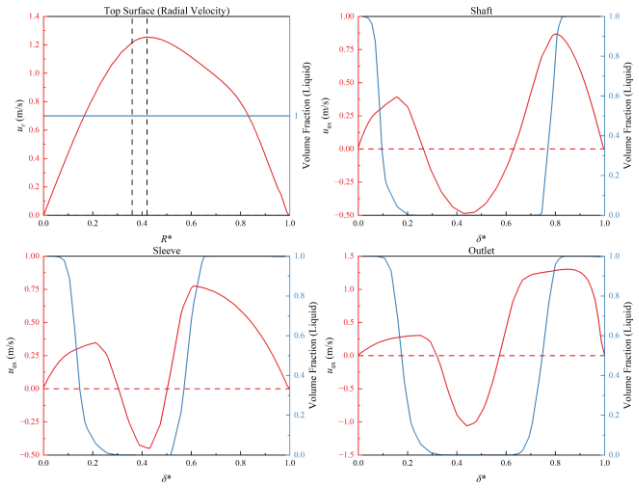

Fig. 10 Distributions of axial velocity and liquid volume fraction

A pronounced air backflow develops within the hollow shaft, with the maximum reverse velocity of approximately 0.5 m/s occurring at $\delta^* = 0.43$. It is noteworthy that not all gas flows upstream: air adjacent to the liquid phase—either along the pipe wall or the inner shaft wall—is entrained by the downward-moving liquid, while only the core region exhibits reverse flow. This phenomenon suggests a stratified gas recirculation structure driven by the pressure gradient established by rotation.

Within the sleeve section, the liquid layer near the sleeve wall becomes thicker, reducing the space available for the recirculating gas. However, near the outlet, the liquid film is centrifugally expelled from the wall, decreasing the local film thickness. The backflowing air accelerates in this region, reaching a velocity of up to 1 m/s. The combined action of centrifugal and pressure-driven effects leads to a helical air recirculation pattern inside the rotating hollow shaft.

The tangential velocity and liquid volume fraction distributions at 4 representative positions are presented in *Fig. 9*. The results reveal a clear coupling between the centrifugal and rotational effects, resulting in distinct Taylor-Couette-type profiles characterized by high tangential velocity near the wall and rapid decay toward the core. At the top surface, the liquid flow is fully developed and dominated by the centrifugal motion. The dimensionless tangential velocity increases monotonically with R^*, indicating a laminar-like shear profile induced by wall rotation.

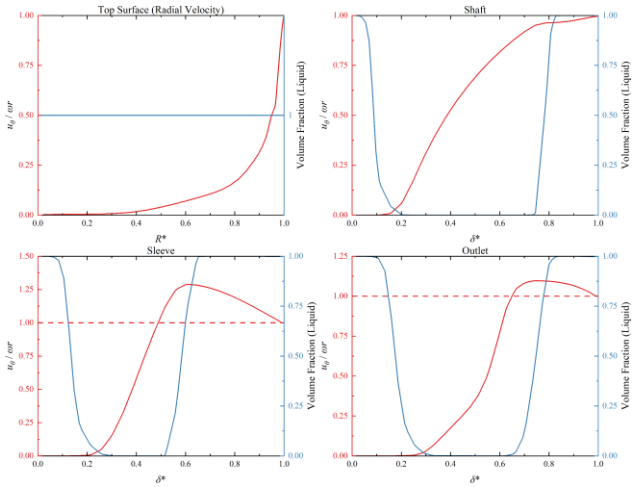

Fig. 9 Distributions of tangential velocity and liquid volume fraction

In the shaft region, a pronounced gas-liquid stratification occurs. The liquid film adjacent to the wall rotates nearly at the wall speed, whereas the gas core exhibits a steep velocity drop, leading to a large interfacial shear. This shear layer is responsible for momentum transfer from the rotating liquid film to the enclosed gas phase. Within the sleeve section, as the flow passes through the contracted cross-section, the

wall-bounded liquid layer is further accelerated, resulting in $u_\theta/\omega r > 1$ near the wall due to centrifugal intensification of the tapered tube.

3.3 Comparative Discussion between Stationary and Rotating Cases

A direct comparison between the stationary and rotating hollow shafts reveals that rotation significantly alters both the flow structure and phase distribution inside the shaft.

In the stationary case, the flow is primarily governed by the momentum of the impinging jet and gravity. The oil jet impacts the top surface, producing a localized pressure peak. However, in the absence of centrifugal force, the liquid momentum is insufficient to drive the fluid radially along the top wall. As a result, the oil detaches prematurely and descends along the sidewall, entraining air and forming a liquid-gas two-phase flow. The entrained gas accumulates near the top corner, leading to incomplete displacement of the initial air phase. Additionally, at the junction between the contraction and the tapered sleeve, a local pressure drop induces cavitation. The outlet region features gas recirculation caused by the pressure imbalance between the shaft and the surrounding vacuum environment.

In contrast, the rotating case exhibits flow behavior dominated by centrifugal effects. The imposed rotation assists the oil in spreading evenly along the top wall and suppresses the near-wall backflow observed under stationary conditions. The centrifugal force drives the liquid toward the sidewall, forming an annular flow pattern where the liquid adheres to the wall and the gas phase concentrates at the core. The gas and liquid phases are clearly separated, and the pressure field becomes smoother, reducing the likelihood of cavitation at the sleeve junction. Nevertheless, a low-pressure region still forms along the shaft axis, which induces a helical air recirculation inside the core.

The velocity field comparison highlights the distinct flow mechanisms. In the stationary case, the flow is characterized by irregular two-phase mixing and weak circulation, with pressure-driven flow dominating. In the rotating case, the tangential and axial components become strongly coupled. The liquid film along the wall reaches near-wall rotational velocity ($u_\theta/\omega r \approx 1$), while the gas core develops a counter-rotating or low-speed zone, typical of Taylor-Couette-Poiseuille flow regimes. This transition from pressure-driven to rotation-dominated flow enhances flow uniformity, stabilizes the liquid film, and significantly reduces air retention inside the shaft.

Overall, the introduction of rotation transforms the internal flow pattern from a chaotic, entrained two-phase structure to an organized annular configuration with stratified gas recirculation and reduced cavitation risk.

4. CONCLUSIONS

A comprehensive numerical study was conducted to investigate the multiphase flow characteristics within a hollow rotating shaft under near-vacuum conditions. The results provide insights into the effects of rotation on flow structure, phase distribution, and pressure evolution.

In the stationary shaft, the impinging jet forms a localized high-pressure region at the top surface, followed by a downward flow dominated by gravity and inertial effects. The flow exhibits strong air entrainment, incomplete air removal, and local cavitation near the sleeve junction. The internal flow pattern remains unstable, with limited recirculation and pronounced phase mixing.

When the shaft rotates at 1000 rpm, centrifugal force becomes the primary driving mechanism. The oil spreads smoothly over the top surface, and the flow organizes into an annular structure, with liquid adhering to the wall and air confined to the core. The air backflow forms a helical recirculation path within the low-pressure core region.

Rotation suppresses near-wall backflow, reduces gas retention, and mitigates cavitation by redistributing the pressure field. The liquid film becomes more stable and continuous along the sidewall, enhancing the overall flow uniformity.

The transition from stationary to rotating operation marks a shift from a pressure-driven, chaotic two-phase regime to a rotation-dominated, stratified flow regime, which is essential for improving the cooling performance and operational stability of hollow rotating shafts in flywheel energy storage systems.

Future work will focus on extending the present model toward experimental validation and broader operational conditions. Additional simulations covering a wider range of rotational speeds (500–2000 rpm) and inlet flow rates will be performed to establish scaling correlations for flow stability and liquid film continuity. Furthermore, coupling the present flow model with conjugate heat transfer (CHT) analysis will enable quantitative evaluation of heat removal efficiency and strengthen the link between internal multiphase flow behavior and the actual thermal performance of flywheel rotors.

ACKNOWLEDGEMENT

The authors gratefully acknowledge the financial support for this research from the National Key R&D Program of China under Grant [2024YFE0208100].

REFERENCE

[1] The National Energy Administration of China. (2025). *China's New Energy Storage Development Report 2025*. [Online] Available: https://www.nea.gov.cn/20250731/1d40d09f75714280a9218d5bea178fbd/202507311d40d09f75714280a9218d5bea178fbd_453d9a0609da1d4456a8b12d843bd256cf.pdf

[2] K. R. Pullen, *Flywheel energy storage* (Storing energy). Elsevier, 2022, pp. 207-242.

[3] A. Gupta and V. Shukla, "Flywheel Energy Storage Market Size - By Application, Analysis, Share, Growth Forecast, 2025 - 2034," USA: Global Market Insights Inc. 4 North Main Street, Selbyville, Delaware, 2025. Accessed: 2025-05-23. [Online]. Available: https://www.gminsights.com/industry-analysis/flywheel-energy-storage-market

[4] P.-O. Gronwald and T. A. Kern, "Traction motor cooling systems: A literature review and comparative study," *IEEE transactions on transportation electrification,* vol. 7, no. 4, pp. 2892-2913, 2021, doi: 10.1109/TTE.2021.3075844.

[5] J. Yuanyuan, W. Yifei, D. Xingjian, and H. C. Hualiang ZHANG, "Overview of the motor-generator rotor cooling system in a flywheel energy storage system," *Energy Storage Science and Technology,* vol. 12, no. 10, p. 3131, 2023, doi: 10.19799/j.cnki.2095-4239.2023.0261.

[6] F. XU, X. DAI, Y. WANG, D. HU, H. ZHANG, and H. CHEN, "Research progress on permanent magnet machines for flywheel energy storage," *Energy Storage Science and Technology,* vol. 13, no. 10, p. 3423, 2024.

[7] B. Melka, J. Smolka, J. Hetmanczyk, and P. Lasek, "Numerical and experimental analysis of heat dissipation intensification from electric motor," *Energy,* vol. 182, pp. 269-279, 2019, doi: 10.1016/j.energy.2019.06.023.

[8] Q. He, J. W. Wang, K. S. Li, X. S. Wang, Z. H. Xu, and Y. B. Zhang, "Thermal analysis and thermal management of high power density electric motors for aircraft electrification," *Applied Thermal Engineering,* vol. 260, Feb 2025, Art no. 125006, doi: 10.1016/j.applthermaleng.2024.125006.

[9] Z. Y. Xu, Y. M. Xu, Y. H. Gai, and W. H. Liu, "Thermal Management of Drive Motor for Transportation: Analysis Methods, Key Factors in Thermal Analysis, and Cooling Methods-A Review," *Ieee Transactions on Transportation Electrification,* vol. 9, no. 3, pp. 4751-4774, Sep 2023, doi: 10.1109/tte.2023.3244907.

[10] A. Meseguer and F. Marques, "On the stability of medium gap corotating spiral Poiseuille flow," *Physics of Fluids,* vol. 17, no. 9, 2005.

[11] C. Leclercq, B. Pier, and J. F. Scott, "Temporal stability of eccentric Taylor-Couette-Poiseuille flow," *Journal of fluid mechanics,* vol. 733, pp. 68-99, 2013.

[12] M. Charmiyan, A. M. Hashemi, A. Joodaki, and F. Aloui, "Numerical investigation of axial flow effects on Taylor-Couette instability: influence of cylinder radius ratios and stabilization mechanisms," *Journal of the Brazilian Society of Mechanical Sciences and Engineering,* vol. 46, no. 10, p. 594, 2024.

[13] S. Poncet, S. Viazzo, and R. Oguic, "Large eddy simulations of Taylor-Couette-Poiseuille flows in a narrow-gap system," *Physics of Fluids,* vol. 26, no. 10, 2014.

[14] T. Çoşgun and N. Vardar, "Combined Effects of Axial Flow and High System Rotation on the Fluid Dynamics of Taylor-Couette-Poiseuille Flow," *Journal of ETA Maritime Science,* vol. 12, no. 3, pp. 332-345, 2024.

[15] G. Luo, Z. Yao, and H. Shen, "Mechanism of pressure oscillation in Taylor-Couette-Poiseuille flow with abruptly contracting and expanding annular gap," *Physics of Fluids,* vol. 31, no. 7, 2019.

[16] L. Gaied, F. Aloui, and L. Keirsbulck, "Experimental study of the effect of a wavy surface in Taylor-Couette-Poiseuille flow," 2021.

[17] J.-S. Yoo, "Mixed convection of air between two horizontal concentric cylinders with a cooled rotating outer cylinder," *International journal of heat and mass transfer,* vol. 41, no. 2, pp. 293-302, 1998.

[18] M. Hadžiabdić, K. Hanjalić, and R. Mullyadzhanov, "LES of turbulent flow in a concentric annulus with rotating outer wall," *International journal of heat and fluid flow,* vol. 43, pp. 74-84, 2013.

[19] R. A. Verschoof, D. Bakhuis, P. A. Bullee, S. G. Huisman, C. Sun, and D. Lohse, "Air cavities at the inner cylinder of turbulent Taylor-Couette flow," *International journal of multiphase flow,* vol. 105, pp. 264-273, 2018.

[20] A. M. Teamah and M. S. Hamed, "Investigation of transient multiphase Taylor-Couette flow," *Alexandria Engineering Journal,* vol. 61, no. 4, pp. 2723-2738, 2022.

[21] P. Reinke, M. Schmidt, and T. Beckmann, "The cavitating taylor-couette flow," *Physics of Fluids,* vol. 30, no. 10, 2018.

[22] R. Wang, X. Fan, D. Li, R. Qu, Z. Liu, and L. Li, "Comparison of heat transfer characteristics of the hollow-shaft oil cooling system for high-speed

permanent magnet synchronous machines," *IEEE Transactions on Industry Applications,* vol. 58, no. 5, pp. 6081-6092, 2022.
[23] W. Pan, J. Ma, Q. Zhang, and H. Su, "Jet impingement cooling in rotating flywheel energy storage systems: Turbulent flow reorganization and shear-layer dominated heat transfer enhancement," *Applied Thermal Engineering,* vol. 270, p. 126238, 2025.
[24] F. R. Menter, M. Kuntz, and R. Langtry, "Ten years of industrial experience with the SST turbulence model," *Turbulence, heat and mass transfer,* vol. 4, no. 1, pp. 625-632, 2003.
[25] L. Könözsy, "The k-ω shear-stress transport (SST) turbulence model," in *A new hypothesis on the anisotropic reynolds stress tensor for turbulent flows: volume i: theoretical background and development of an anisotropic hybrid k-omega shear-stress transport/stochastic turbulence model*: Springer, 2019, pp. 57-66.
[26] F. R. Menter, "Review of the shear-stress transport turbulence model experience from an industrial perspective," *International journal of computational fluid dynamics,* vol. 23, no. 4, pp. 305-316, 2009.
[27] L. Tantao, G. Limin, and L. Ruiyu, "Experimental Data-Driven Flow Field Prediction for Compressor Cascade based on Deep Learning and ℓ1 Regularization". *Journal of Thermal Science*, 2024, 33(5): 1867-1882.